3D Investigation of Damage During Strain-Controlled Thermomechanical Fatigue of Cast Al–Si Alloys

Katrin Bugelnig,* Holger Germann, Thomas Steffens, Robert Koos, Elodie Boller, Fabian Wilde, and Guillermo Requena

The strain-controlled thermomechanical fatigue behavior is investigated for three cast near-eutectic Al–Si alloys with different Ni, Cu, and Mg contents. Synchrotron tomography and neutron diffraction experiments are used to correlate 3D microstructural features with damage initiation and evolution. The results show that the alloy with lower Cu, Ni, and Mg concentrations has up to 45% higher thermomechanical fatigue resistance for cooling/heating rates of 5 and 15 K s^{-1}. In addition, this alloy also exhibits damage formation at later stages during thermomechanical fatigue and slower damage accumulation compared to other alloys. This difference in behavior is a consequence of its higher ductility, which is a result of the lower volume fraction and global interconnectivity of the 3D hybrid networks formed by Si and intermetallics and the absence of large primary Si clusters which act as preferred crack initiation sites during the early stages of thermomechanical fatigue.

1. Introduction

Cast near-eutectic Al–Si alloys are widely used for combustion engine pistons owing to their light weight, low manufacturing costs, excellent castability, wear resistance, low thermal expansion, high specific strength, and recyclability.[1–4] The continuous efforts to increase the efficiency of combustion engines, pushed by environmental regulations, are leading to thermomechanical conditions at the limits of operability of cast Al–Si piston alloys.[5,6] For instance, complex stress conditions induced by short thermal cycles over temperature ranges between room temperature (RT) and ≈380 °C can result in the formation of damage at the microscale that rapidly propagates through brittle microstructural constituents. Therefore, these alloys must exhibit high-temperature stability while retaining sufficient ductility to avoid the premature failure of pistons.[1,7–10]

The composition of cast Al–Si piston alloys is characterized by a near-eutectic Si concentration (≈10–13 wt%) and <10 wt% of other alloying elements such as Ni, Cu, Mg. This results in a microstructure formed by interconnected 3D hybrid networks of eutectic and primary Si and intermetallic phases embedded in a comparatively soft age-hardenable α-Al matrix.[11–15] Methods such as microstructural modification through adjustments in chemical composition[16–20] and changing the cooling rate during casting[21] can be employed to improve the thermomechanical fatigue (TMF) resistance of piston alloys. In general, coarse microstructures are more susceptible to damage initiation,[22] whereas refined microstructures achieved by high solidification rates can significantly enhance the TMF performance of cast Al–Si alloys.[3,10,22] An extreme example of this is the excellent thermal shock resistance of the fine microstructure generated by laser melting in the bowl rim area of pistons.[10]

Previous investigations of the high-temperature strength of Al–Si piston alloys with different Ni, Cu, Fe, and Mg concentrations revealed that the interconnectivity of the eutectic Si is highly conserved after solution treatment. A comparison between a binary AlSi$_{12}$ alloy and an AlSi$_{12}$Ni$_1$ alloy revealed ≈50% higher strength

K. Bugelnig, G. Requena
Institute for Materials Research
German Aerospace Centre
Linder Höhe, 51147 Cologne, Germany
E-mail: katrin.bugelnig@dlr.de

H. Germann, T. Steffens
Rheinmetall Automotive AG
Karl-Schmidt-Straße, 74172 Neckarsulm, Germany

The ORCID identification number(s) for the author(s) of this article can be found under https://doi.org/10.1002/adem.202300339.

R. Koos
FRM II
Forschungs-Neutronenquelle Heinz Maier-Leibnitz
Technische Universität München, 85748 Garching, Germany

E. Boller
ESRF, European Synchrotron Radiation Facility
CS40220, Cedex 9 Grenoble, France

F. Wilde
Helmholtz-Zentrum Hereon
Zentrum für Material- und Küstenforschung GmbH
Max-Planck-Straße 1, 21502 Geesthacht, Germany

G. Requena
Metallic Structures and Materials Systems for Aerospace Engineering
RWTH Aachen University
52062 Aachen, Germany

**ADVANCED
SCIENCE NEWS**

www.advancedsciencenews.com

**ADVANCED
ENGINEERING
MATERIALS**

www.aem-journal.com

at 300 °C and ≈30% longer TMF life for the Ni-containing alloy. This improved TMF performance was linked to the load-carrying capacity of the hybrid 3D networks.[11,13,14] These networks are affected by topological and morphological changes, such as spheroidization of Si particles and partial dissolution of Mg_2Si and/or Al_2Cu intermetallics during thermal heat treatments and/or service conditions.[7,11,23–25] It has also been shown that a reduction of the interconnectivity of the 3D networks has a direct impact on the mechanical performance of the alloys.[11,14,23,26,27]

The dominant damage mechanisms in cast near-eutectic Al–Si alloys depend on the test temperature during deformation: while damage initiation at RT was observed to be exclusively associated with fracture of primary Si particles (preferentially at clusters of primary Si particles).[28–33] Decohesion at Si/Al–matrix interfaces and void formation in Al become relevant at elevated temperatures.[16,29,33–35] Although postmortem 2D and 3D investigations show cracks in primary Si particles and aluminides, the damage sequence in Al–Si alloys during TMF remains unsolved.[20] Efforts in this direction have been made for other alloy systems. For example, Wang et al. used in situ synchrotron X-ray tomography to investigate damage mechanisms in an extruded magnesium alloy under uniaxial low-cycle fatigue with ratcheting.[36]

The aim of this study is to investigate the effects of microstructural parameters on the TMF resistance, in particular damage initiation and accumulation, for different cast near-eutectic Al–Si alloys. The investigations are carried out using synchrotron microtomography in combination with conventional metallography and complemented by neutron diffraction experiments. In addition, thermodynamic calculations based on the CALPHAD method are performed to shed light on the influence of the chemical composition on the observed microstructural differences and the resulting TMF behavior.

2. Results

2.1. Microstructure

Representative light optical micrographs are shown in **Figure 1**: All alloys show a microstructure consisting of bulky primary and plate-like eutectic Si (dark grey) and aluminides (light gray) embedded in the α-Al matrix. Qualitatively, the micrographs show that 1232 (see Figure 1a) presents a larger fraction of eutectic Si as well as smaller primary Si particles than 12 421 and 12 431. Moreover, 12 421 and 12 431 reveal the presence of large primary Si clusters (see Figure 1b,c) that were not observed in the microstructure of 1232.

Table 1 presents the hardness of the alloys determined by Brinell hardness and of the α-Al matrix determined by nanoindentation.

Table 1. Hardness of the alloys (HB) and of the matrix (H) for each investigated alloy.

Alloy	HB (1/10)	H [GPa]
1232	105.6 ± 2.3	1.46 ± 0.11
12421	126.2 ± 2.77	1.77 ± 0.14
12431	128.5 ± 1.38	1.83 ± 0.11

Alloys with higher Cu, Ni, and Mg contents, that is, 12 421 and 12 431, show a Brinell hardness of 126.2 ± 2.77 HB and 128.5 ± 1.38 HB, respectively, while that of 1232 is about 20% lower. The latter alloy also has the lowest matrix hardness, that is, 1.46 ± 0.11 GPa, owing to the lower Mg and Cu concentrations.

Figure 2 shows 3D visualizations of microstructural constituents present in the investigated alloys.

The bottom of these volumes displays aluminides (red), eutectic Si (green), and primary Si (blue). The rest of the volumes show the hybrid 3D network (Si + aluminides) formed by these phases, with the largest 3D network shown in blue at the top right (different colors were assigned to each isolated particle in this region). A video of the 3D microstructure of all investigated alloys is provided in the supplements.

A quantitative analysis of the 3D hybrid networks reveals volume fractions, V_f, ranging from ≈21 to 27 vol% (**Figure 3**, yellow bars). The global interconnectivity, I, (Figure 3, aquamarine bars) is ≈89–92% for 12 421 and 12 431, while 1232 presents a comparatively lower I of ≈74%. This is also consistent with the lower Brinell hardness measured in this alloy (≈20% lower than 12 421 and 12 431), as this parameter depends on the fraction of hard phases, their interconnectivity, and the precipitation state of the matrix.[37,38]

The connectedness, calculated by the Euler characteristic of the largest hybrid 3D network in the investigated volume (**Figure 4**, pink bars), shows the most negative value for 12 431 ($\chi = -34\,706 \pm -1735$), indicating the highest connectedness of the hybrid 3D network among all investigated alloys. This can be attributed to the high Ni content, which results in the formation of a large number of plate-like Ni-rich aluminides during solidification that act as interconnecting branches within the 3D networks.[39] 1232 displays a higher connectedness ($\chi = -26\,444 \pm -1322$) than 12 421 although it has a lower global interconnectivity.

The size of primary Si particles and their spatial distribution is shown in **Figure 5**. The left side of the volumes shows individual particles color coded by size, while the right side shows clusters of connected primary Si particles.
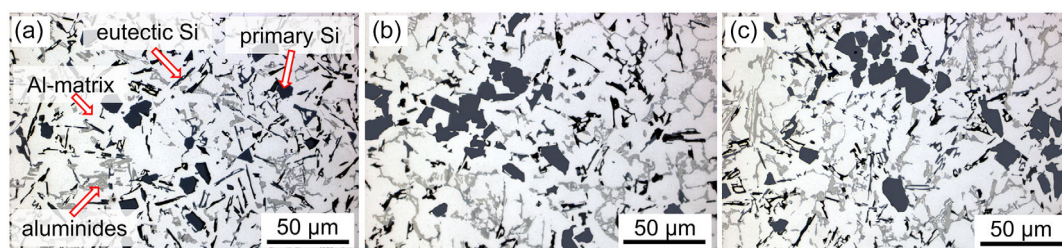

Figure 1. Light optical micrographs of the initial microstructure: a) 1232, b) 12 421, c) 12 431.
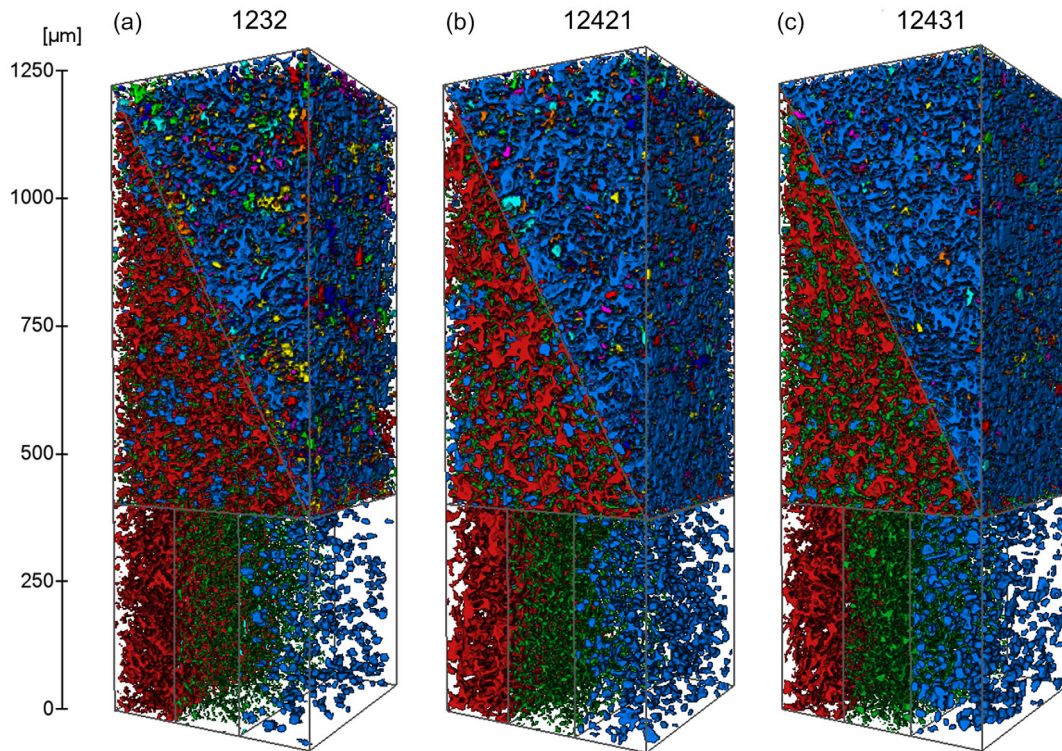
Figure 2. 3D visualization of microstructure constituents (three sections of bottom part: aluminides = red, eutectic Si = green, primary Si = blue), hybrid network (upper left part), and interconnectivity (upper right part: A different color was assigned to each isolated particle) for a) 1232, b) 12 421, c) 12 431.
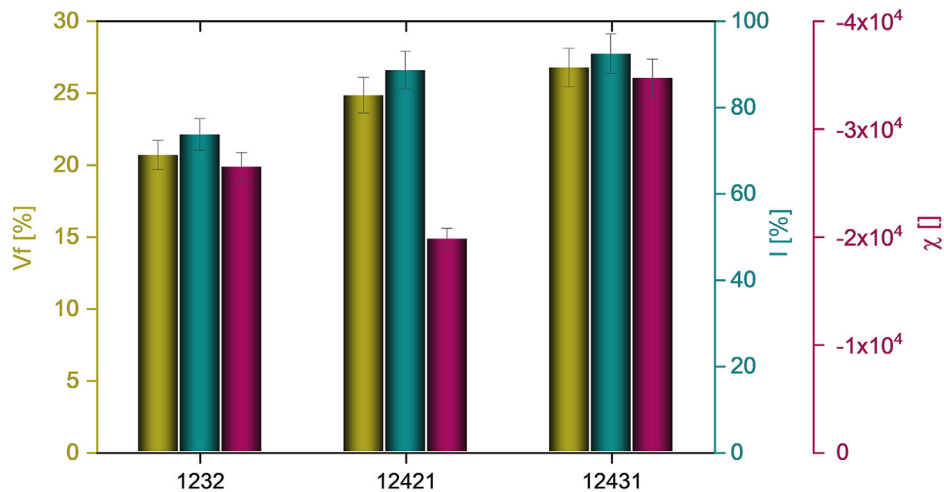

Figure 3. Quantitative descriptors of the 3D hybrid networks: volume fraction, V_f, global interconnectivity I, connectedness, χ, calculated using the Euler characteristic.

The alloy 1232 shows the lowest volume fraction and the smallest size of primary Si as well as a low number of Si particle clusters (Figure 4a), whereas the number of clusters and their size is significantly higher for 12 421 and 12 431 (see Figure 4b,c). Moreover, the clusters are distributed heterogeneously throughout the volumes.

A quantification of the size distribution of primary Si reveals smaller particle sizes for 1232 (mean particle size = $1824 \pm 1654\ \mu m^3$), while 12 421 and 12 431 present rather similar mean particle sizes of 2993 ± 9070 and $3077 \pm 6118\ \mu m^3$, respectively.

2.2. Thermomechanical Fatigue

Figure 5 shows representative stress–temperature (σ–T) hysteresis loops obtained during the strain-controlled TMF tests for the

**ADVANCED
SCIENCE NEWS**

www.advancedsciencenews.com

**ADVANCED
ENGINEERING
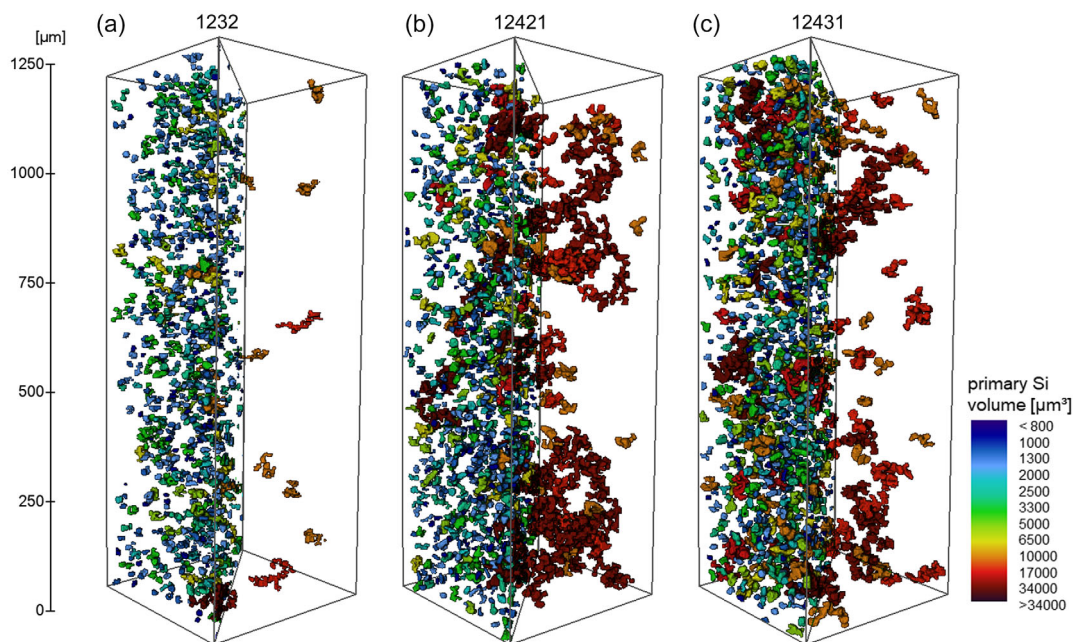MATERIALS**

www.aem-journal.com

Figure 4. 3D visualization of primary Si particles: a) 1232, b) 12 421, and c) 12 431. The left side of the volumes shows all primary Si particles; the right side of the volumes shows primary Si particles and clusters colour coded according to their size.
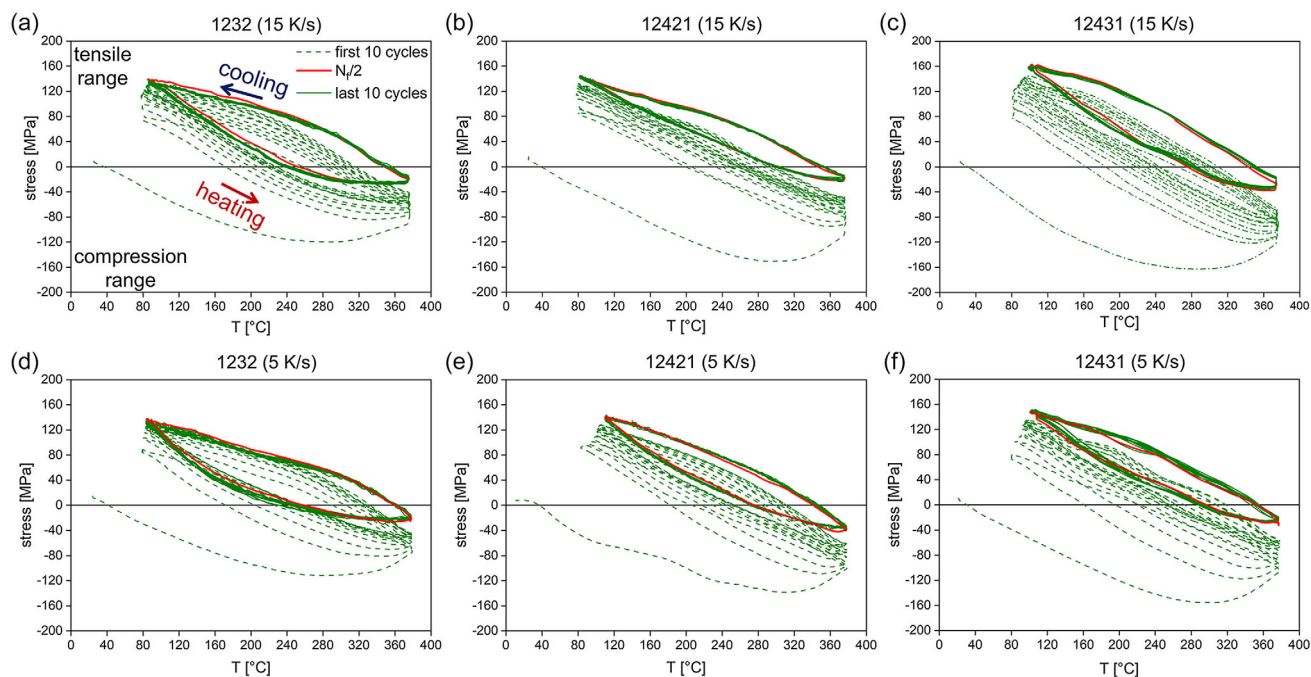

Figure 5. σ–T hysteresis loops obtained during strain-controlled TMF experiments: a,d) 1232, b,e) 12 421, c,f) 12 431 for heating/cooling rate a–c) 15 K s^{-1} and d–f) 5 K s^{-1}.

first ten thermal cycles, the thermal cycle at half-life ($N_f/2$), and the last ten thermal cycles. The results for 5 and 15 K s^{-1} heating/cooling rates are shown in Figure 5a–f, respectively.

Compressive stresses build up fairly linearly until about 200 °C during the heating period of the first cycle, reaching a maximum compressive stress of about −120 to −160 MPa for

all studied alloys and heating rates. Thereafter, stress relaxation takes over until the maximum temperature (380 °C) is reached and the first cooling period begins. During this stage, the stresses gradually change from compressive to tensile reaching a maximum tensile stress at the end of the thermal cycle. Qualitatively, the stress–temperature behavior of the subsequent
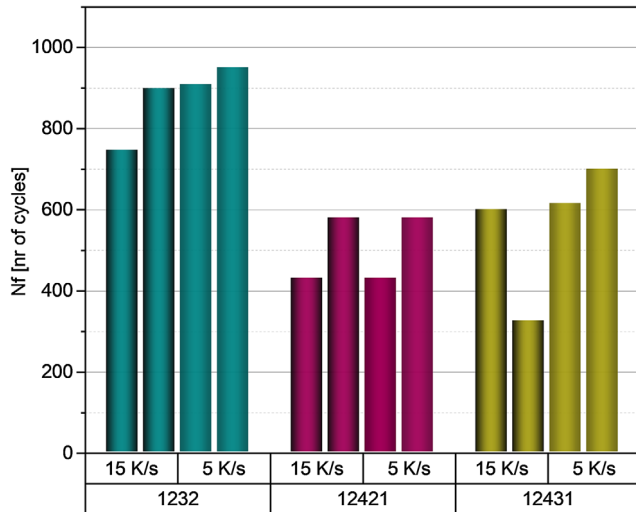
Figure 6. Number of cycles to failure.

the TMF tests indicates a cyclic softening of the alloys at high temperatures.

Figure 6 shows the number of thermal cycles to failure, N_f, for each alloy. The 1232 alloy shows the longest TMF life for both heating/cooling rates. N_f for 1232 is about 39% and 45% higher than for 12421 and 12431 at 15 K s^{-1}, respectively. The slower heating/cooling rate does not affect significantly the TMF life for 1232 and 12421, while it results in an increase of 32% for 12431 compared to 15 K s^{-1}.

Figure 7 shows the evolution of maximum tensile (σ_{maxT}) and compressive stresses (σ_{maxC}) reached in each cycle during TMF as well as the stress amplitude ($\Delta\sigma$). All three parameters show a fast increase during the first ≈100 TMF cycles, followed by fairly stationary evolution until failure. While in general the maximum stresses tend to increase slightly in the stationary period, σ_{maxT} shows a slight decrease for 1232 for both heating/cooling rates. This indicates cyclic softening for 1232 and slight cyclic hardening for the other alloys investigated. The difference in behavior may be a consequence of the lower volume fraction and global interconnectivity of the 3D hybrid network observed for 1232, which allows higher ductility at lower temperatures but, as a trade-off, comparatively lower strength at elevated temperatures.

The analysis of damage evolution in the following sections focuses on the 15 K s^{-1} TMF tests as this is closer to the service conditions of the alloys.

2.2.1. 3D Characterization of Damage Formation and Accumulation

Figure 8 shows characteristic damage mechanisms observed at different stages of TMF. The results shown correspond to 12421 and are representative for the three alloys investigated.

The initial microstructure is shown in the synchrotron X-ray tomography (sXCT) slice in Figure 8a). TMF-induced damage initiation was found already after the first thermal cycle in the form of microcracks (Figure 8b). The 3D visualizations show

thermal cycles is similar, except for a shift of the hysteresis loops in the vertical direction (toward higher tensile stresses), whereas the relaxation period at $T > 200\,°C$ becomes less pronounced as the number of thermal cycles increases. The vertical shift of the hysteresis loops is more marked during the first ten thermal cycles (dotted lines in Figure 5) and continues through the first 80–100 thermal cycles, followed by a relatively stationary σ–T loop until failure (see solid lines in Figure 5). Fracture of the specimens always occurs under tension at the highest tensile loading condition of the last cycle. The alloys 12421 and 12431 build up slightly larger stresses than 1232.

The vertical shift of the hysteresis loops indicates a hardening of the alloys during TMF and has also been reported in other studies.[40,41] At the same time, the vertical shift of the stress reached at the highest temperature (380 °C) observed throughout
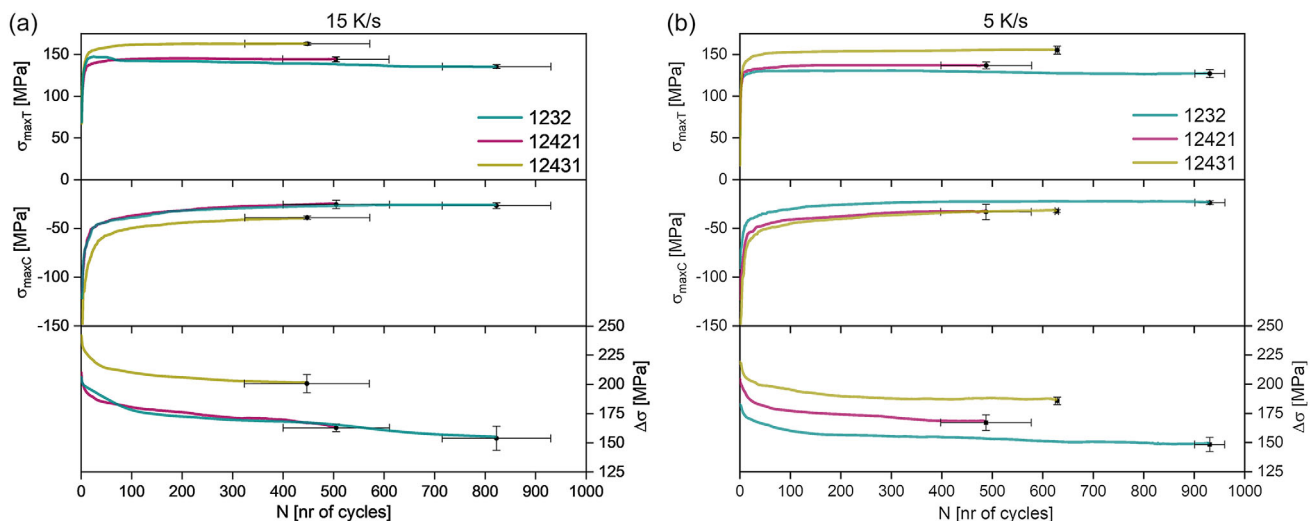

Figure 7. Evolution of maximum tensile stresses (σ_{maxT}), maximum compression stresses (σ_{maxC}), and stress amplitudes ($\Delta\sigma$) for each cycle during TMF for cooling /heating rates a) 15 K s^{-1} and b) 5 K s^{-1}.
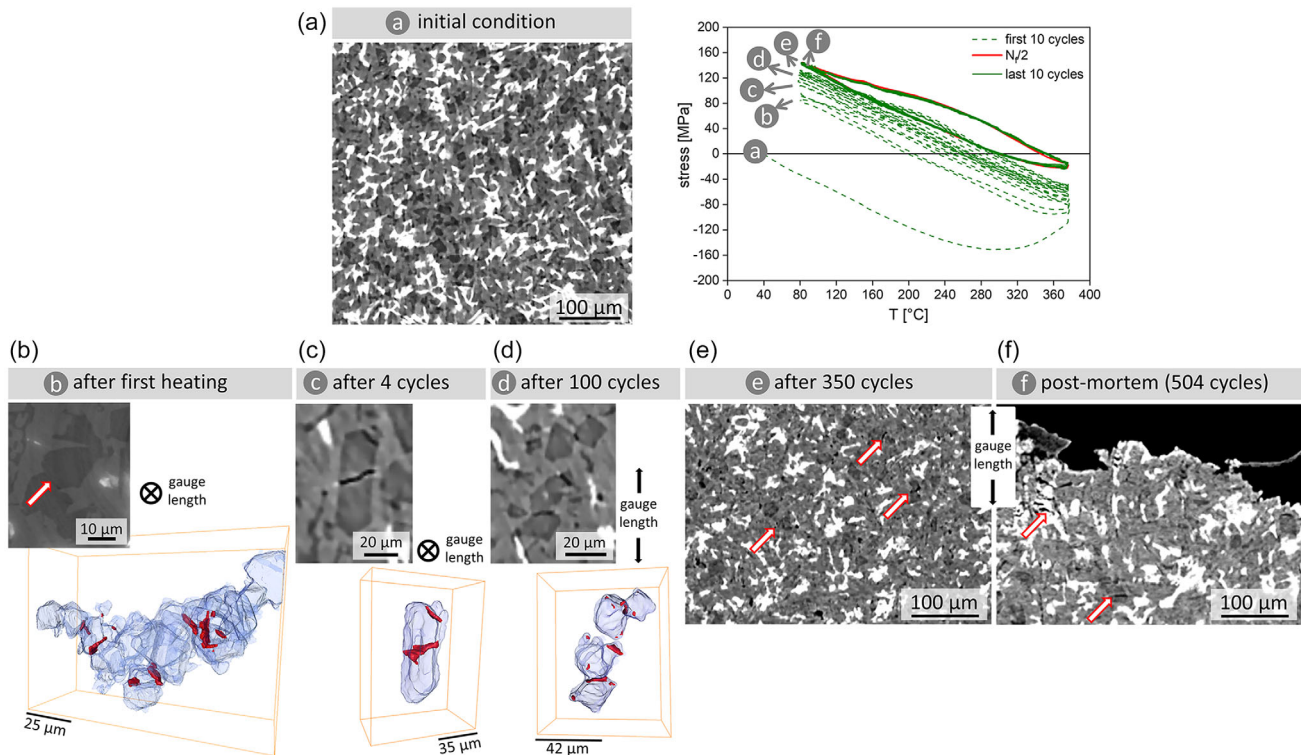
Figure 8. Representative 2D and 3D images of microstructure and damage mechanisms in the alloy 12 421 (microcracks (red), primary Si clusters blue): a) initial condition, b) after one thermal cycle, c) after four thermal cycles, d) after 100 TMF cycles, e) shortly before failure, and f) postmortem.

primary Si in blue and microcracks in red. These microcracks are mostly located at the junctions between coalesced primary Si particles and are oriented parallel to the sample gauge length, as shown in Figure 8b,c. This was also observed for 12 431. On the other hand, 1232 showed no damage after the first cycle, whereas microcracks were observed only after the fourth thermal cycle. The fact that the microcracks in the early stages of TMF are oriented parallel to the sample gauge length indicates that they are the result of superimposed microscopic stresses induced by the mismatch of thermal expansion coefficients between the Al matrix and the embedded rigid phases and macroscopic compressive stresses induced by the restricted thermal expansion of the sample during the heating process (see $\sigma-T$ curve in Figure 8, especially the first ten cycles, i.e., dotted lines). Since maximum tensile stresses are induced perpendicularly to the gauge length, microcracks form perpendicular to the stress direction.

The earlier damage initiation in 12 421 and 12 431 can be attributed to the higher global interconnectivity of the rigid 3D networks and the presence of larger amounts of primary Si clusters. In general, similar damage mechanisms were observed for all investigated alloys. As the thermal cycles progress, the formation of microcracks oriented perpendicular to the sample gauge length becomes relevant, indicating that damage also occurs in tensile mode, that is, during the cooling phase of the thermal cycles (see Figure 8d). Further accumulation of damage can be observed after 100 thermal cycles, particularly in large, irregularly shaped clusters of primary Si particles, where

microcracking through junctions, fracture of sharp edges, and decohesion at the Si/Al–matrix interfaces were observed (Figure 8d). Damage then continues accumulating until their coalesce leads to final failure (see Figure 8e,f). Voids within the matrix could also be observed after 100 cycles. No cracks initiating from porosity formed during casting were detected. Representative images analogues to Figure 8 for the other alloys investigated can be found in the Figure S1 and S2, Supporting Information.

Figure 9 shows the evolution of number density of voids (n_{voids}) and voids volume fraction (Vf_{voids}) as a function of thermal cycle number (N). Corresponding 3D visualizations of the investigated volumes can be found in the Supporting Information (Figure S3).

Analysis of the sXCT data shows that 1232 has a lower number and volume fraction of voids than the other alloys for the same number of cycles. Only 12 431 shows a significant decrease in both number density and volume fraction of voids between the last step before failure and the postmortem state. This can be explained by the fact that the 3D data were obtained from ex situ measurements, that is, a different sample was scanned for each selected cycle number.

Lattice Strains as a Function of TMF: **Figure 10** shows the evolution of lattice strains in the gauge length direction for Al, Si, and Al_7Cu_4Ni determined by neutron diffraction as a function of thermal cycle number. The lattice strains were determined with respect to the initial condition before the TMF experiments. While tensile strains tend to build up during
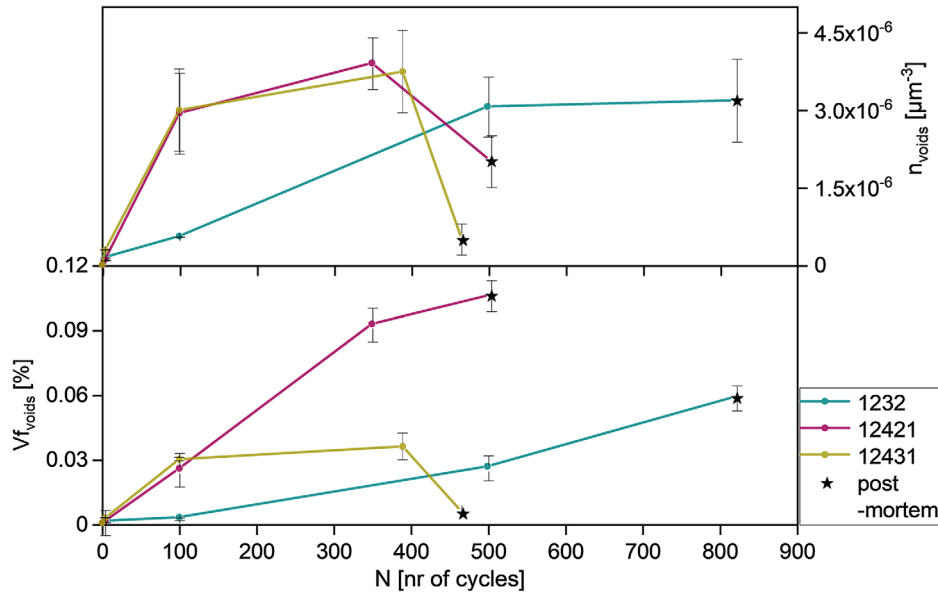
Figure 9. Number density and volume fraction of voids after selected thermal cycle numbers cooling-/heating rate: 15 K s^{-1}). The star symbols indicate the postmortem condition.
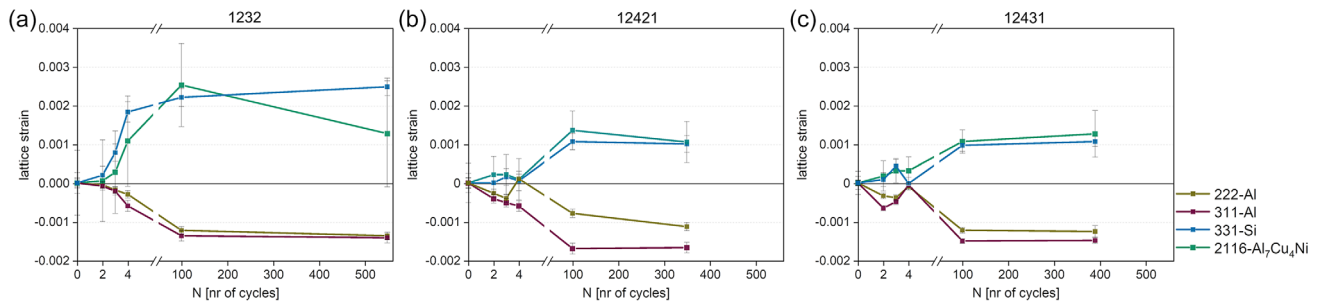
Figure 10. Lattice strains as a function of thermal cycle number for heating/cooling rate = 15 K s^{-1}: a) 1232, b) 12 421, and c) 12 431.

TMF for Si and Al$_7$Cu$_4$Ni, the Al lattice shows compressive strains. A clear increase in the lattice strains of Si and Al$_7$Cu$_4$Ni can be observed after four thermal cycles for alloys 12 421 and 12 431(Figure 10b,c), whereas the alloy 1232 shows a continuous increase in lattice strains already from the second thermal cycle onward. The lattice strains remain fairly constant after 100 thermal cycles, with the strains in 1232 reaching more than twice the strain of the other alloys.

3. Discussion

The damage behavior during TMF of all three alloys investigated is strongly linked to the primary Si phase, its morphology, and spatial distribution. Damage initiated for all alloys as microcracks through primary Si in the early stages of TMF, while microcracks continued to form and accumulate through Si and intermetallics as well as at the interface between the matrix and hybrid 3D networks. Additionally, voids within the Al–matrix could be observed at later stages during TMF. These observations are

in agreement with Wang et al.[18,20] who investigated the thermal cyclic fatigue behavior of Al–Si alloys over a temperature range of 120–425 °C. They found that damage initiates by primary Si cracking induced by dislocation pile-up at lower temperatures and debonding at the interfaces between matrix and Si or intermetallics induced by vacancy accumulation at elevated temperatures. The formation of voids in the matrix and at interfaces between matrix and Si or intermetallics during mechanical loading at elevated temperatures has also been reported in several studies.[13,33]

Our investigations also reveal that the stage of damage initiation depends on the composition of the alloys studied: While 12 421 and 12 431 show damage initiation already after the heating period of the first thermal cycle, the damage in the 1232 alloy was first observed after the fourth thermal cycle. In addition, damage accumulation is slower for the 1232 alloy. This is also consistent with the neutron diffraction results, which show higher Si lattice strains for the 1232 alloy after 100 cycles, whereas 12 421 and 12 431 accumulate only about half the lattice strain. This difference is likely due to a larger stress relief in

12 421 and 12 431, as evidenced by the larger fraction of microcracks through primary Si particles.[38] This may be related to the higher TMF lifetime observed for 1232, expressed as number of cycles to failure, which is about 40% and 45% higher than for 12 421 and 12 431 at 15 K s^{-1}. Compared to 12 421 and 12 431, the 1232 alloy has smaller primary Si particles, a lower fraction of primary Si clusters, as well as a lower volume fraction and global interconnectivity of the 3D hybrid network. In contrast to tensile strength, which largely depends on the connectedness of the 3D hybrid network in these alloys,[26,39] the TMF resistance is also influenced by microstructural features such as the size and morphology distribution of primary Si, the volume fraction, and global interconnectivity of the hybrid network. The lower global interconnectivity in 1232 allows accommodating a higher degree of plastic deformation in the Al matrix, while it partially hinders propagation and merging of microcracks.[26,39] The isolated primary Si particles in 1232 are also favorable for TMF because clusters of coalesced primary Si can act as favorable sites for damage initiation (Figure 8). Similar observations have been reported for different types of external loading.[26,39,42]

In light of these results, a detailed quantification of primary Si cluster size distributions was carried out to reveal their influence on the TMF behavior. The clusters were classified into groups of different criticality according to our previous investigations:[39] Based on morphological observations, primary Si particles can be classified into four groups with different 3D volume (V_{primSi}) ranges: 1) single particles ($V_{prim\ Si} \leq 3500\ \mu m^3$); 2) small primary Si clusters ($3500\ \mu m^3 \leq V_{prim\ Si} \leq 7000\ \mu m^3$); 3) larger clusters with up to about 15 connected particles ($7000\ \mu m^3 \leq V_{prim\ Si} \leq 10\ 000\ \mu m^3$); and 4) very large primary Si clusters with volumes above $10\ 000\ \mu m^3$. Among these groups, the last one was observed to have the greatest impact on damage initiation. We have therefore divided group 4 into three classes which are also visualized on the right side of the 3D visualizations in Figure 4: Class 1 corresponds to clusters with $10\ 000\ \mu m^3 \leq V_{prim\ Si} \leq 17\ 000\ \mu m^3$, class 2 are clusters with $17\ 000\ \mu m^3 \leq V_{prim\ Si} \leq 34\ 500\ \mu m^3$, and class 3 comprises clusters $>34\ 500\ \mu m^3$.

Figure 11 shows triangle diagrams that correlate the volume fraction of primary Si, Vf_{Si}, Si content, the volume fraction of primary Si clusters, Vf_{class}, and the relative volume fraction of the clusters with respect to the volume fraction of primary Si, $Vf_{Si-class}$.

The volume fraction of primary Si clusters is defined for each cluster as

$$Vf_{class\ i} = V_{class\ i}/V_{ROI} \tag{1}$$

where $Vf_{class\ i}$ is the volume fraction of clusters within the investigated volume, i indicates the class, $V_{class\ i}$ is the total 3D volume of Si clusters, and V_{ROI} is the 3D volume of the investigated volume. The relative volume fraction of primary Si clusters with respect to the total volume of primary Si is defined for each cluster as

$$Vf_{Si-class\ i} = V_{class\ i}/V_{primSi} \tag{2}$$

where $Vf_{Si-class\ i}$ is the volume fraction of clusters within the investigated volume and $V_{prim\ Si}$ is the total 3D volume of primary Si particles in the investigated volume.

The volume fraction of clusters $>10\ 000\ \mu m^3$ is similar for 12 421 and 12 431 alloys at about 1.4 vol%. Alloy 1232 has a volume fraction of only about 0.1 vol% of such clusters with respect to the investigated volume. In addition, alloy 1232 has the lowest proportion of class 1 and 2 clusters and no class 3 clusters. On the other hand, 12 431 presents the highest fraction of class 1 and 2 clusters, whereas 12 421 is the alloy with the largest fraction of class 3 clusters. These differences are clearer for the relative volume fraction of Si clusters, $Vf_{Si-class\ i}$, and are an evidence of the dominating role of primary Si particles in damage accumulation during TMF: The large, irregularly shaped and brittle structures formed by the Si clusters induce earlier damage and a faster damage accumulation during TMF.

CALPHAD simulations were carried out to shed light on the microstructural differences observed by s-XCT and they were shown to play a relevant role for TMF resistance. **Figure 12**a) shows the calculated solidification interval for the investigated alloys based on the change in volume of the system during solidification. The rectangles in Figure 12a) indicate the following regions of interest: blue, complete solidification of the alloys; red, solidification onset of the Al–matrix; green, formation of primary Si particles.

The solidification of primary Si starts at ≈595 °C for 12 431, while for 12 421 and 1232 it begins at about 10 °C lower temperatures, that is, ≈583 and ≈581 °C, respectively (green rectangle). In addition, the solidus temperature of 12 431 and 12 421 are
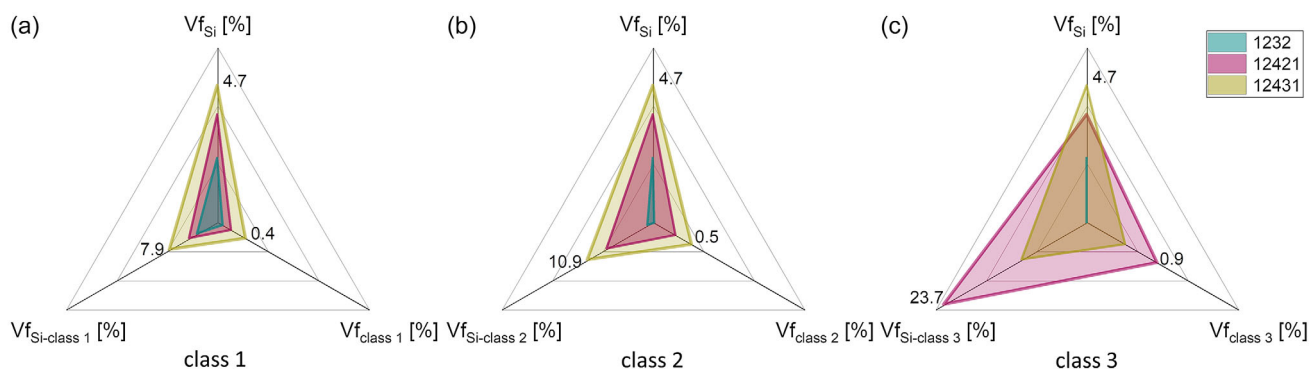

Figure 11. Si content, volume fraction of clusters as well as of relative volume fraction of clusters with respect to the volume fraction of primary Si of a) class 1, b) class 2 and c) class 3.
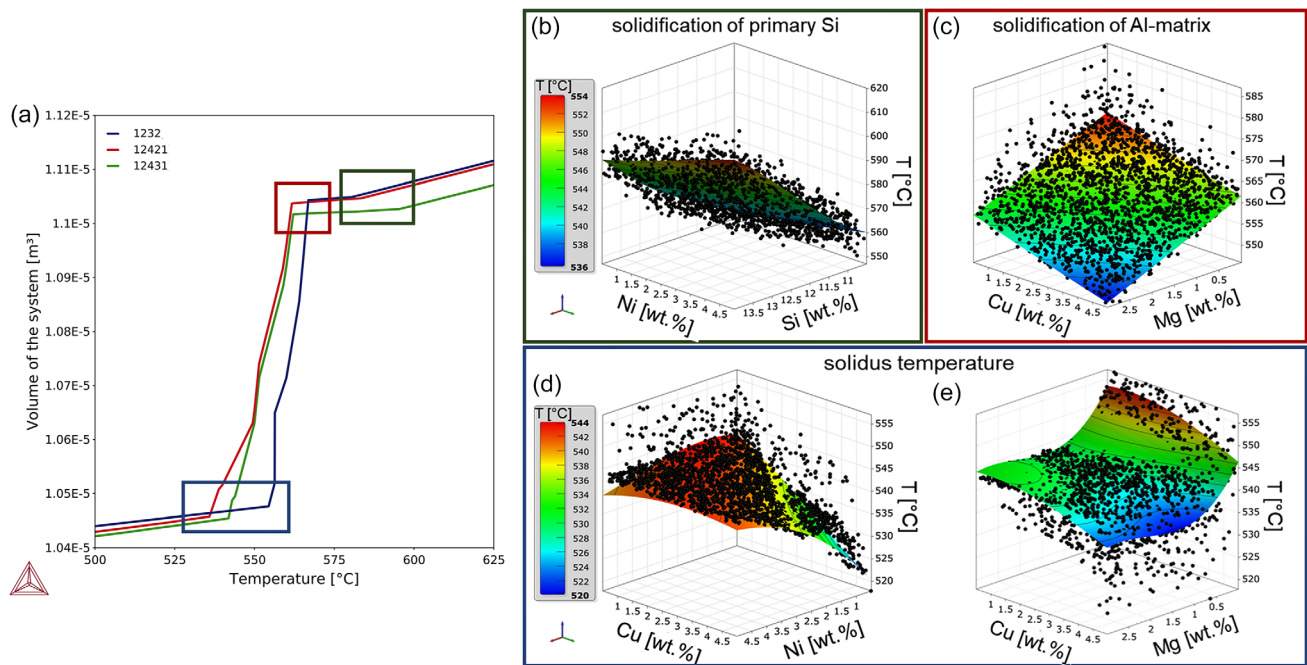
Figure 12. a) Solidification intervals identified based on the change in system volume, b) influence of alloying elements Ni and Si on the solidification temperature of primary Si, c) influence of Cu and Mg content on solidification temperature of the Al-matrix, d,e) induence of Cu , Mg and Ni on the solidus temperature.

$\approx$542 and $\approx$536 °C, respectively, whereas 1232 has the highest solidus temperature of $\approx$555 °C (blue rectangle). This indicates that the solidification ranges of 12 421 and 12 431 ($\approx$47 and $\approx$53 °C) are $\approx$50% larger than for 1232 ($\approx$26 °C).

In order to understand which elements are responsible for differences in solidification intervals and the onset of solidification of phases described above, a sensitivity analysis was carried out using the software OptiSlang in combination with Thermo-Calc. To this purpose, the solidification intervals and solidification temperature of primary Si and Al were calculated for 2500 compositions varying the concentration of Ni, Cu, and Mg. The solidification temperature of primary Si (Figure 12b) and Al (Figure 12c) as well as the solidus temperature are shown in Figure 12b–e as a function of the concentration of alloying elements. The black dots indicate individual chemical compositions, while the colored area is the response surface, showing the correlation between the alloying elements (input parameters) and the calculated solidus and phase solidification temperatures (output parameters) as obtained using the adaptive response surface methodology (see Section 2.4).

Figure 12b reveals the correlation between Si and Ni content and the solidification temperature of primary Si. Nucleation of primary Si starts at earlier stages (higher temperature), the higher the Ni concentration. Thus, alloy 12 431 has an earlier onset of primary Si solidification and shows an even wider solidification range (see Figure 12a) compared to 12 421. In addition, the solidus temperature increases with the Ni content (see Figure 12d), which explains the slight increase of the solidus temperature for 12 431 with respect to 12 421 ($\approx$1 wt% less Ni).

Moreover, Cu and Mg have a clear influence on the solidus temperature (see Figure 12e) and the solidification temperature

of Al (see Figure 12c). Lower concentrations of Cu and Mg result in the solidification of the Al–matrix at higher temperatures and a higher solidus temperature. This can be attributed to the absence of late-forming phases such as Mg_2Si and the Q-phase $Al_5Cu_2Mg_8Si_6$, as well as the lower amount of θ–Al_2Cu owing to the lower Cu content.[43] This also explains the significantly shorter solidification interval of 1232.

Summarizing, higher Ni, Cu, and Mg concentrations lead to a larger solidification interval. The resulting longer solidification ranges for the 12 421 and 12 431 alloys facilitate the formation of chain-like primary Si. On the other hand, the shorter solidification interval of 1232 limits the growth of microstructural constituents and restricts the formation of primary Si clusters.

4. Conclusion

The strain-controlled TMF behavior of three cast near-eutectic Al–Si alloys with varying Cu, Ni, and Mg contents has been investigated with respect to the influence of 3D microstructural features on damage formation and evolution. The following conclusions can be drawn from the analysis of the results. 1) The alloy 1232 shows superior TMF resistance due to its higher ductility enabled by a lower volume fraction and global interconnectivity of the hybrid 3D network as well as by the presence of smaller primary Si clusters compared to the other alloys; and 2) The sequence of damage is similar for all the investigated alloys. In the early TMF stages microcracks form parallel to the sample length at large primary Si clusters. These microcracks accumulate with increasing TMF cycles, while additional microcracks form perpendicular to the sample length beyond

**ADVANCED
SCIENCE NEWS**

www.advancedsciencenews.com

**ADVANCED
ENGINEERING
MATERIALS**

www.aem-journal.com

Table 2. Labeling and chemical composition of investigated alloys.

Alloy	Labeling	Approximate chem. composition [wt%]				
		Al	Si	Cu	Ni	Mg
AlSi12Cu3Ni2	1232	bal.	12.3	≈3	≈2	<1
AlSi12Cu4Ni2Mg	12421	bal.	12.5	≈4	≈2	≈1
AlSi12Cu4Ni3Mg	12431	bal.	13.1	≈4	≈3	≈1

100 thermal cycles. Final failure occurs by coalescence of damage of microcracks through Si and aluminides. The onset of damage in 1232 occurs later and at a lower rate of accumulation than in 12421 and 12431.

As a general conclusion, large volume fractions of highly interconnected rigid phases can lead to a high tensile strength of the alloy at elevated temperatures, but this is accompanied by low ductility at low temperatures, which limits TMF resistance. On the other hand, microstructures with isolated primary Si particles and less primary Si clusters have a positive effect on TMF resistance.

5. Experimental Section

Materials: Three cast near-eutectic Al–Si alloys with varying contents of Cu, Ni, and Mg were investigated. **Table 2** shows the chemical composition of the alloys. These are identified hereafter by the designations 1232, 12421, and 12431 for $AlSi_{12}Cu_3Ni_2$, $AlSi_{12}Cu_4Ni_2Mg$, and $AlSi_{12}Cu_4Ni_3Mg$, respectively.

All samples were extracted from the bowl rim area of pistons produced by gravity die casting by Kolbenschmidt GmbH. After casting, the alloys were subjected to aging at 230 °C for 5 h followed by air cooling.

Thermomechanical Fatigue: TMF was investigated using the thermomechanical simulation system Gleeble 1500.[44,45] Strain-controlled TMF experiments that mimicked the thermal cycles caused by the change from idle-running to full-throttle engine conditions were conducted. For this, the strain of cylindrical samples (see **Figure 13**a) was kept constant at 0% (strain-controlled), while the stress generated by thermal cycles between 80 and 380 °C was measured using a load cell.

Dwelling segments of ten and three seconds, respectively, were applied after reaching the minimum and maximum temperatures (the temperature profile is shown in Figure S4, Supporting Information). Figure 13b shows a schematic illustration of the experimental setup. The strain was monitored using an inductive strain gauge. Heating was achieved by an electrical current passing through the sample, while cooling was supported by compressed air using a U-shaped quenching device around the sample. An actual picture of the TMF setup is shown in Figure S5, Supporting Information. A fast and a slow heating/cooling rate of 15 and 5 K s^{-1} were used. The temperature was controlled using a thermocouple welded to the sample. The samples were mounted with their threads coated in Ni-base lubricant to reduce stress fluctuations during the experiments. Furthermore, a small compressive preforce of about −0.4 kN was applied at RT before thermal loading. At least two TMF experiments were carried out for each alloy under the same conditions.

The stress amplitude ($\Delta\sigma$) and the mean stress (σ_m) during TMF were computed according to[46]

$$\Delta\sigma = \sigma_{max} - \sigma_{min} \qquad (3)$$

$$\sigma_m = \frac{(\sigma_{max} + \sigma_{min})}{2} \qquad (4)$$

Microstructure Characterization: The initial microstructure was characterized by light optical microscopy (LOM) and scanning electron microscopy (SEM). Furthermore, the microhardness of the alloys was evaluated by Brinell-hardness HB 1/10 tests while the hardness of the Al matrix was measured using a UMIS Nanoindentation System 2K0A. Further details can be found in our previous works.[26,39]

The low number density of damage sites (tensile fracture strain of the alloys is <5%) makes the study of damage by 2D metallography of interrupted TMF samples unreliable. Thus, complementary 3D characterization of the microstructure and the damage evolution was conducted by sXCT at the beamlines ID19 of the European Synchrotron Radiation Facility (ESRF) in Grenoble, France,[47] and P05 of the synchrotron source PETRA III of DESY in Hamburg, Germany, operated by the Helmholtz–Zentrum
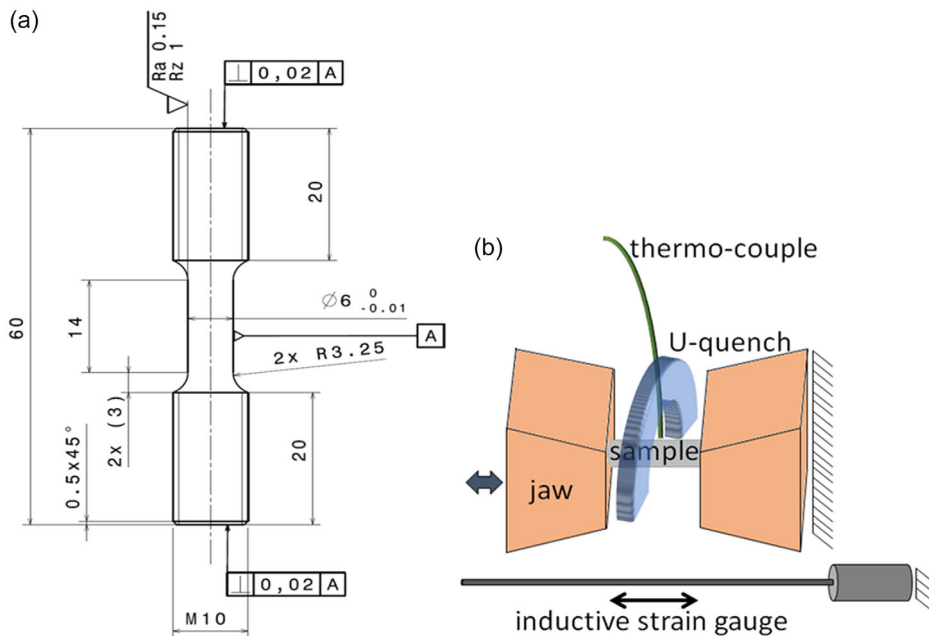

Figure 13. a) Sample geometry and b) schematic illustration of the experimental setup for the TMF tests.

**ADVANCED
SCIENCE NEWS**

www.advancedsciencenews.com

**ADVANCED
ENGINEERING
MATERIALS**

www.aem-journal.com

Table 3. Parameters for sXCT at P05 & ID 19.

Beamline	Camera	E [keV]	FOV [mm²]	Sample-to-detector distance [mm]	Nr. of proj.	Exposure time [msec proj⁻¹]	Voxel size [μm³]	Total scan time [h]
P05 DESY	CCD	23	$(1.775)^2$	30	900	1200	$(1.18)^3$	1.5
ID19 ESRF	PCO Edge 5.5	19	$(0.7)^2$	13	5969	100	$(0.325)^3$	0.2

Hereon.[48] Cylindrical specimens with a diameter of 0.6 mm were investigated in the following conditions: 0 (initial condition), 1, 4, 100 thermal cycles, shortly before failure and postmortem. **Table 3** shows the parameters for the sXCT scans. Two consecutive overlapping scans were performed at the centre of the gauge length for each sample.

Preprocessing and Image Segmentation: The software Fiji[49] was used for converting the reconstructed tomographs into a more processing-friendly format, that is, tif images with 8 or 16 bit. Preprocessing to filter ring artefacts was also carried out using Fiji applying a polar transformation and bandpass filter, stack normalization followed by image enhancement with standard filters such as 3D median filter (radius = 1 pixel), and a 2D anisotropic diffusion filter (5–10 iterations). Further image enhancement using the Filter Sandbox tool and tools such as Beam Hardening Correction as well as 3D visualizations were done using the software Avizo Fire versions 8.1 to 2021.1.

Segmentation was performed with Avizo for small regions with only selected features of interest using gray-level thresholds with manual corrections. For large representative volumes and considering all microstructural constituents, a convolutional neural network with a U-Net architecture[50] was used, which was implemented and modified in a previous work by the authors to meet the needs of the Al–Si alloys studied.[51]

Quantitative Evaluation of the 3D Microstructure and Damage: The 3D analysis of the initial microstructure was carried out for reconstructed sXCT volumes of ≈420 × 400 × 1180 μm³ (voxel size = (1.18 μm)³). The 3D parameters volume fraction, V_f, global interconnectivity, I, and connectedness, χ, expressed by the Euler characteristic, were evaluated for the 3D hybrid networks in each investigated alloy.[52–54] As defined in our previous works, the global interconnectivity of a phase was quantified as the volume of the largest particle divided by the total volume of all particles of the same phase in the studied volume.[14] The Euler characteristic is a topological parameter that analyzes the interconnecting branches within a 3D network.[53] Furthermore, the size distribution of primary Si particle clusters was calculated. These parameters and their evaluation are described in detail in our previous works.[26,39]

The volume fraction and number density of voids were quantified for volumes of ≈590 × 590 × 1180 μm³ (voxel size = (1.18 μm)³), while the smallest void volume considered was 10 μm³.

Neutron Diffraction: Neutron diffraction was carried out at the angle-dispersive strain scanner *Stress Spec* of the high-flux neutron source FRM II in Munich, Germany[55,56] which is also partly operated by the Helmholtz–Zentrum Hereon. Lattice strains were measured after the same number of TMF cycles as in the tomography experiments.

The neutron diffraction experiments were carried out using a monochromatic beam with a wavelength $\lambda = 1.669$ Å (Si(400) monochromator), a sample-to-detector distance of 1035 mm, and a 2θ interval of 82°–94°. A 2D position-sensitive detector (PSD) with a size of 256 × 256 pixel and 300 × 300 mm² was used. The strains were determined in the longitudinal direction of the samples (Figure 1a) using a gauge volume of 5 × 5 × 5 mm³ and an acquisition time of 3600 s. Rocking of the samples in a range of ±3° was applied to reduce the effect of texture and grain size.

The lattice strains were evaluated for the 331–Si, 311–Al, 222–Al, and 2116–Al₇Cu₄Ni reflections.[38,57] The diffraction peak of 2116–Al₇Cu₄Ni was weak and overlapped with 222–Al; therefore, the lattice strains could not be estimated in all cases for this reflection. The lattice strains are computed according to

$$\varepsilon = \frac{(d - d_0)}{d_0} \tag{5}$$

where ε indicates the lattice strain, d_0 is the lattice spacing in the initial condition at ambient temperature before TMF, and d is the lattice spacing after thermal cycling.

Thermodynamic Calculations: Solidification simulations were conducted using the thermodynamic calculations software Thermo-Calc 2021a[58] using the TCAl7 database for Al in combination with the optimization software OptiSlang 8.1.0.[59]

A Python interface was used to link the simulation and optimization softwares. This approach was used to determine the correlation between a set of input parameters, in our case the alloying elements, and a set of response variables, in this case the alloy properties calculated in Thermo-Calc. A sensitivity analysis was performed to quantify the importance of the design variables on the model responses. For this purpose, Space filling Latin Hypercube Sampling was used to define 2500 initial designs with varied chemical compositions for which solidus and phase solidification temperatures were to be calculated. Once a corresponding response value was obtained for each alloy design, sensitivity was measured as correlation coefficients and polynomial-based coefficients of importance are estimated.[59] In this work, the results of this analysis were presented in the form of 3D response surface plots with superimposed support points indicating the calculated alloy designs. They showed the approximated values for the selected response or objective data function with respect to the two selected input parameters.

These calculations were carried out to shed light on the origin of the microstructures of the studied alloys as a function of chemical composition, especially as a function of Ni, Cu, and Mg contents and their interaction with Si.

Supporting Information

Supporting Information is available from the Wiley Online Library or from the author.

Acknowledgements

Conflict of Interest

The authors declare no conflict of interest.

Author Contributions

K.B. performed the experiments, analyzed the data, contributed to interpretation and discussion, and wrote the manuscript. H.G. and T.S. contributed to design the project, provided material resources, and contributed to discussion of results. F.W. and E.B. supported with acquiring and 3D reconstructing the synchrotron tomography data. R.K. acquired

and processed neutron diffraction data. G.R. conceived and designed the project, contributed to interpretation, discussion, and writing of the paper. All authors reviewed the manuscript.

Data Availability Statement

Research data are not shared.

Keywords

cast Al–Si alloys, neutron diffraction, synchrotron tomography, thermomechanical fatigue, 3D microstructure characterizations

[1] M. Javidani, D. Larouche, *Int. Mater. Rev.* **2014**, *59*, 132.

[2] J. R. Davies, *ASM Special Handbook: Aluminium and Aluminium Alloys*, ASM International, Victor, NY **1993**, ISBN: 978-0-87170-496-2.

[3] L. Tian, Y. Guo, J. Li, F. Xia, M. Liang, Y. Bai, *Materials* **2018**, *11*, 1230.

[4] K. Morimoto, H. Takamiya, Y. Awano, M. Nakamura, *J. Jpn. Inst. Light Met.* **1988**, *38*, 779.

[5] The European Parliament and the Council of the European Union, *Directive 2000/53/EC of the European Parliament and of the Council of 18 September 2000 on End-of-Life Vehicles*, Official Journal of the European Communities **2000** pp. 34–42.

[6] S. Spangenberg, T. Hettich, M. Lazzara, K. Scherer, *35th Internationales Wiener Motorensymposium* **2014**, pp. 204-216.

[7] F. S. Silva, *Eng. Fail. Anal.* **2006**, *13*, 480.

[8] G. Floweday, S. Petrov, R. B. Tait, J. Press, *Eng. Fail. Anal.* **2014**, *18*, 1664.

[9] G. Nicoletto, E. Riva, A. Di Filippo, *Procedia Eng.* **2014**, *74*, 157.

[10] C. Otto, *Neuer Aluminium-Kolben für Hochleistungs-Dieselmotoren*, e-paper, Automobil-Industrie, **2012**, 368505.

[11] G. Requena, G. Garcés, Z. Asghar, E. Marks, P. Staron, P. Cloetens, *Adv. Eng. Mater.* **2011**, *13*, 674.

[12] R. Fernández Gutiérrez, F. Sket, E. Maire, F. Wilde, E. Boller, G. Requena, *J. Alloys Compd.* **2017**, *697*, 341.

[13] Z. Asghar, G. Requena, *Mater. Sci. Eng., A* **2014**, *591*, 136.

[14] Z. Asghar, G. Requena, E. Boller, *Acta Mater.* **2011**, *59*, 6420.

[15] R. Fernández-Gutiérrez, G. Requena, *Mater. Sci. Eng., A* **2014**, *598*, 147.

[16] M. R. Joyce, C. M. Styles, P. A. S. Reed, *Int. J. Fatigue* **2003**, *25*, 863.

[17] Z. Wenda, Y. Jing, D. Jingzhi, L. Yun, X. Hong, *Adv. Mater. Res.* **2013**, *652–654*, 1030.

[18] M. Wang, J. C. Pang, H. Q. Liu, S. X. Li, Z. F. Zhang, *J. Mater. Res. Technol.* **2022**, *8*, 4556.

[19] K. Liu, S. Wang, P. Hu, L. Pan, X.-G. Chen, *Materials* **2023**, *16*, 3515.

[20] M. Wang, J. Pang, X. Liu, J. Wang, Y. Liu, S. Li, Z. Zhang, *Materials* **2022**, *15*, 7113.

[21] M. Zamani, S. Seifeddine, M. Azuzuderourei, *TMS Light Metals 2013*, (Ed. B. Sadler), Hoboken, NJ **2013**, pp. 297–302.

[22] M. Zamani, S. Seifeddine, A. E. W. Jarfors, *Mater. Des.* **2015**, *86*, 361.

[23] D. Tolnai, G. Requena, P. Cloetens, J. Lendvai, H. P. Degischer, *Mater. Sci. Eng., A* **2013**, *585*, 480.

[24] M. A. Moustafa, F. H. Samuel, H. W. Doty, *J. Mater. Sci.* **2003**, *38*, 4507.

[25] A. M. A. Mohamed, F. H. Samuel, *INTECH* **2012**.

[26] K. Bugelnig, F. Sket, H. Germann, T. Steffens, R. Koos, F. Wilde, E. Boller, G. Requena, *Mater. Sci. Eng., A* **2018**, *709*, 193.

[27] R. Koos, *PhD Thesis*, Technical University of Vienna, Austria **2014**.

[28] S. K. Shaha, F. Czerwinski, W. Kasprzak, J. Friedman, D. L. Chen, *Int. J. Fatigue* **2015**, *70*, 383.

[29] M. Lebyodkin, A. Deschamps, Y. Bréchet, *Mater. Sci. Eng., A* **1997**, *234–236*, 481.

[30] M. A. Moustafa, F. H. Samuel, H. W. Doty, *J. Mater. Sci.* **2003**, *38*, 4523.

[31] T. O. Mbuya, P. A. S. Reed, *Mater. Sci. Eng., A* **2014**, *612*, 302.

[32] A. Gangulee, J. Gurland, *Trans. Metall. Soc. AIME* **1967**, *239*, 269.

[33] J. Feng Su, X. Nie, V. Stoilov, *Mater. Sci. Eng., A* **2010**, *527*, 7168.

[34] G. Zhang, J. Zhang, B. Li, W. Cai, *Prog. Nat. Sci.: Mater. Int.* **2011**, *21*, 380.

[35] M. Wang, J. Pang, Y. Qiu, H. Liu, S. Li, Z. Zhang, *Adv. Eng. Mater.* **2018**, *20*, 1700610.

[36] Z. Wang, S. Wu, G. Kang, H. Li, Z. Wu, Y. Fu, P. J. Withers, *Acta Mater.* **2021**, *211*, 116881.

[37] G. C. Requena, P. Degischer, E. D. Marks, E. Boller, *Mater. Sci. Eng., A* **2008**, *487*, 99.

[38] M. Schöbel, G. Baumgartner, S. Gerth, J. Bernardi, M. Hofmann, *Acta Mater.* **2014**, *81*, 401.

[39] K. Bugelnig, H. Germann, T. Steffens, F. Sket, J. Adrien, E. Maire, E. Boller, G. Requena, *Materials* **2018**, *11*, 1300.

[40] H. J. Christ, V. Bauer, *J. Phys. Conf. Ser.* **2010**, *240*, 012038.

[41] M. H. Wilfried Wunderlich, *Int. J. Mater. Mech. Eng.* **2012**, *1*, 57.

[42] S. Joseph, S. Kumar, *Mater. Sci. Eng., A* **2013**, *588*, 11.

[43] L. F. Mondolfo, *Aluminum Alloys: Structures and Properties*, Butterworth &Co (Publishers) Ltd, London, GB **1976**.

[44] Gleeble 1500 System, https://www.gleeble.com/products/gleeble-systems/gleeble-1500.html, (accessed: November 2021).

[45] J. Qin, D. Racine, K. Liu, X.-G. Chen, *Proc. of the ICAA16*, Canadian Institute of Mining, Metallurgy & Petroleum, Canada **2018**, ISBN: 978-1-926872-41-4.

[46] W. Heinz, *PhD Thesis*, Montan Universität Leoben **2010**.

[47] ESRF ID19 Beamline, http://www.esrf.eu technical university of vienna/home/UsersAndScience/Experiments/StructMaterials/ID19.html, (accessed: June 2023).

[48] F. Wilde, M. Ogurreck, I. Greving, J. U. Hammel, F. Beckmann, A. Hipp, L. Lottermoser, I. Khokhriakov, P. Lytaev, T. Dose, H. Burmester, M. Müller, A. Schreyer, *AIP Conf. Proc.* **2016**, *1741*, 030035.

[49] J. Schindelin, I. Arganda-Carreras, E. Frise, V. Kaynig, M. Longair, T. Pietzsch, A. Cardona, *Nat. Methods* **2019**, *9*, 676.

[50] O. Ronneberger, P. Fischer, T. Brox, *Med. Image Comput. Comput. Assist. Interv. (MICCAI)*, Springer, Switzerland **2015**, pp. 234–241.

[51] T. Strohmann, K. Bugelnig, E. Breitbarth, F. Wilde, T. Steffens, H. Germann, G. Requena, *Sci. Rep.* **2019**, *9*, 19611.

[52] D. B. Aydogan, J. Hyttinen, *J. R. Soc. Interface* **2014**, *11*, 20131042.

[53] A. Kruglova, M. Engstler, G. Gaiselmann, O. Stenzel, V. Schmidt, M. Roland, S. Diebels, F. Mücklich, *Comput. Mater. Sci.* **2016**, *120*, 90.

[54] J. Toriwaki, T. Yonekura, *Forma* **2002**, *17*, 183.

[55] L. Pintschovius, M. Hofmann, *Modern Diffraction Methods*, (Eds: E. J. Mittermeijer, U. Welzel), Wiley-VCH, Weinheim **2012**, pp. 155–172.

[56] M. Hofmann, R. Schneider, G. A. Seidl, J. Rebelo-Kornmeier, R. C. Wimpory, U. Garbe, *Physica B* **2006**, *385–386*; 1035.

[57] B. Clausen, T. Lorentzen, *Metall. Mater. Trans. A* **1997**, *28*, 2537.

[58] J. O. Andersson, T. Helander, L. Höglund, P. F. Shi, B. Sundman, *Calphad* **2002**, *26*, 273.

[59] Ansys-OptiSlang tool, https://www.ansys.com/products/connect/ansys-optislang, (accessed: January 2023).